

1 **A Vertical Equilibrium Model for CO₂ Migration in Depleted**
2 **Gas Fields**

3 Saeid Telvari^{1,*}, Hariharan Ramachandran¹, Gang Wang¹, Florian Doster¹

4 ¹Institute of GeoEnergy Engineering (IGE), School of Energy, Geoscience, Infrastructure
and Society, Heriot-Watt University, Edinburgh, EH14 4AS, UK

*Corresponding author: Saeid Telvari (st4014@hw.ac.uk)

5 **Preprint statement.**

6 This manuscript is a non-peer-reviewed preprint submitted to **EarthArXiv**. It
has been submitted to a peer-reviewed journal for consideration. Subsequent
versions of this preprint may differ in content following peer review; if accepted,
the final version will be available via a *DOI* link on this preprint page. Please feel
free to contact any of the authors with feedback.

7 **ORCID:** <https://orcid.org/0000-0002-4896-295X>

8 **Keywords:** Vertical equilibrium modeling; CO₂ storage; Depleted gas reservoirs; Reser-
voir simulation.

A Vertical Equilibrium Model for CO₂ Migration in Depleted Gas Fields

Saeid Telvari^{1,*}, Hariharan Ramachandran¹, Gang Wang¹, and Florian Doster¹

¹Institute of GeoEnergy Engineering (IGE), School of Energy, Geoscience, Infrastructure and Society, Heriot-Watt University, Edinburgh, EH14 4AS, UK

*Corresponding author: st4014@hw.ac.uk

Abstract

This study extends the vertical equilibrium (VE) modeling framework to simulate multi-phase flow involving CO₂, methane, and brine in depleted gas reservoirs. Methane presence introduces complexity not captured in traditional VE models. The proposed model integrates a black-oil approximation with VE assumptions, reducing dimensionality and enabling rapid simulation of large-scale CO₂ injection. By representing CO₂ and methane as separate compressible phases, and treating brine as incompressible, the model balances computational speed and physical realism. Pressure-dependent density and viscosity relationships for CO₂ and methane enable accurate property estimation without flash calculations. Three case studies validate the model: (1) a flat, layered reservoir benchmark demonstrating accurate CO₂ plume behaviour under buoyancy control; (2) a dual-anticline scenario demonstrating that the VE model reproduces the large-scale plume geometry and inter-anticline mass redistribution observed in compositional simulations; and (3) a field-scale application to the Hugin Formation East, where the VE model replicates key features of CO₂ and methane migration observed in compositional models. The VE model runs orders of magnitude faster than full 3D simulations while capturing large-scale displacement dynamics. Although the formulation neglects explicit mixing, dissolution, and capillary fringe effects, it captures first-order displacement behaviour with speedups of up to two orders of magnitude. This makes it a practical tool for screening, uncertainty quantification, and optimisation in CCS projects targeting depleted gas reservoirs.

Plain Language Summary

Storing carbon dioxide (CO₂) underground in depleted gas reservoirs is a promising way to reduce greenhouse gas emissions. However, predicting how injected CO₂ moves in these reservoirs is difficult because the pore space may still contain natural gas and water, and detailed computer models can be very slow. In this study, we developed a faster modeling approach to simulate how CO₂, methane, and brine move together after CO₂ injection. The method is based on the idea that fluids can quickly arrange themselves vertically under gravity, which allows the model to simplify the problem while still capturing the main large-scale behavior. We tested the method in three cases, from simple idealized settings to a field-scale reservoir model. The results show that the new model reproduces the main migration and trapping patterns seen in much more detailed three-dimensional simulations, while running up to 100 times faster. Although it does not yet include some finer-scale processes such as mixing and dissolution, it captures the dominant flow behavior well. This makes it useful for rapid screening, uncertainty analysis, and planning of carbon storage projects in depleted gas reservoirs.

1 Introduction

Carbon capture, utilization, and storage (CCUS) is a key mitigation strategy for reducing greenhouse gas emissions and supporting global carbon neutrality efforts, particularly for industries that are challenging to decarbonize, including steel, cement, and chemical manufacturing, as well as potential large-scale production of bio-hydrogen [Méndez et al., 2023, Chen et al., 2022, Rosa and Mazzotti, 2022, Wei et al., 2023]. CCUS entails capturing carbon dioxide (CO_2) from industrial emissions or directly from the atmosphere, followed by its transportation for either reuse or permanent underground storage [Krevor et al., 2023, Wareing et al., 2014, Chen et al., 2022, Lau et al., 2021]. One of the most promising methods for permanent CO_2 storage involves injecting it into geological formations such as deep saline aquifers or depleted oil and gas reservoirs [Hepple and Benson, 2004, Kumar et al., 2005, Ringrose et al., 2021, Hamza et al., 2021]. Utilizing depleted oil and gas fields generally offers secure long-term storage, as these formations have retained hydrocarbons beneath impermeable caprocks for millions of years. In some cases, it may also facilitate enhanced hydrocarbon recovery, which can help offset some of the costs related to CO_2 sequestration. Compared to saline aquifers, which can experience pressure build-up and integrity challenges during CO_2 injection, hydrocarbon reservoirs provide a well-documented storage environment with lower pressures and extensive geological data availability. Another significant advantage of depleted reservoirs is the presence of existing infrastructure for CO_2 transport and injection [Hamza et al., 2021, Jenkins et al., 2012, Muhammed et al., 2023, Patel et al., 2016].

A key difference between depleted reservoirs and saline aquifers is the presence of natural gas in depleted gas reservoirs. This adds complexity to the process as contact between CO_2 and the gas causes fluid mixing, leading to the creation of a mixing zone that alters key fluid properties, including density and viscosity, which in turn modifies displacement mechanisms and can induce convective currents that further influence the migration and redistribution of CO_2 and reservoir gas. Therefore, an accurate representation and study of their behavior and interactions are required [Ma et al., 2019, Ghanbari et al., 2020, Liu et al., 2022]. Reservoir simulation serves as a crucial tool for analyzing and studying CO_2 geological storage. Both commercial and open-source simulators are available to represent various scenarios [Class et al., 2009]. To be able to properly define and differentiate CO_2 and natural gas and capture the mixing phenomena, we need to define a multi-component gas phase. Compositional simulations use Equations of State (EoS) to model multi-component behavior in one or more phases. In this context, CO_2 can be accurately differentiated from hydrocarbons, allowing for accurate modeling of their interactions in the reservoir [Oldenburg and Org, 2003, Al-Hashami et al., 2005, Ghanbari et al., 2020, Liu et al., 2022]. Compositional simulations are computationally intensive because they must perform flash calculations in every gridblock, which typically require more iterations for convergence than models that rely on simplified phase behavior representations. Previous research has explored the application of black oil models to simulate thermodynamic phase behavior in compositional simulations in order to speed up the simulations and maintain accuracy as much as possible. This approach sacrifices some accuracy in favor of cost efficiency, making it particularly useful for uncertainty analysis [Hassanzadeh et al., 2008, Amooie and Moortgat, 2018]. Nonetheless, CO_2 storage simulations still remain computationally intensive due to the large spatial scales and extended timeframes spanning several centuries.

In many cases, the horizontal extent of the reservoir is much larger than the vertical. When there is a significant density difference between fluids and sufficient vertical permeability, gravity causes them to segregate, with heavier fluids settling at the bottom and lighter ones rising to the top. This leads to a state of vertical equilibrium (VE), where fluid saturations vary predictably with depth. The vertical equilibrium assumption allows us to integrate the governing equations over the vertical axis and express them in terms of vertically averaged parameters. As a result, we can simplify a 3D model into a 2D one, which greatly reduces computational cost. This

99 approach, referred to as VE modeling, is increasingly used for simulating large-scale CO₂ plume
100 migration in the subsurface [Nordbotten and Celia, 2011, Bandilla et al., 2019]. Traditionally,
101 VE models applied to CO₂ storage problems have focused on two-phase systems, where the
102 reservoir is initially saturated with brine and CO₂ is injected as a single immiscible gas phase.
103 The most common simplification in early VE models involved complete segregation of fluids with
104 a distinctive interface [Gasda et al., 2009, Nilsen et al., 2016b, Court et al., 2012]. These models
105 have since been extended to include effects such as hysteresis [Doster et al., 2012, 2013, Gasda
106 et al., 2013b], heterogeneity [Guo et al., 2016, Moyner and Nilsen, 2019], dissolution [Gasda et al.,
107 2011, Mykkeltvedt and Nordbotten, 2012], capillary fringe [Nilsen et al., 2016a, Nordbotten and
108 Dahle, 2011], sub-scale topographic variations (rugosity) [Gasda et al., 2012, 2013a, Ahmadiania
109 et al., 2019], fault leakage [Ramachandran et al., 2024], geomechanics [Bjørnarå et al., 2016,
110 Andersen et al., 2017], compressibility [Andersen et al., 2015], and fractured (dual-continuum)
111 reservoirs [March Castaneda Neto, 2018, Guo et al., 2017, Tao et al., 2019]. Additionally,
112 several studies have aimed to relax the assumption of vertical equilibrium for wider applications,
113 including near-wellbore flow, well leakage, and large-scale plume migration in heterogeneous
114 formations [Guo et al., 2014, 2016, Becker et al., 2017, Zheng et al., 2021]. To address the
115 limitations of VE models, particularly near injection wells and heterogeneous reservoir regions,
116 other researchers have explored hybrid approaches that couple between VE and 3D models
117 [Moyner and Nilsen, 2019, Becker et al., 2022, Buntic et al., 2025].

118 The computational efficiency of VE models makes them particularly valuable for screening
119 studies and statistical analysis workflows that require the simulation of large ensembles. In carbon
120 storage assessment, uncertainty quantification demands evaluation across numerous geological
121 realizations, injection scenarios, and operational parameters—tasks that become computationally
122 impractical with full-physics compositional models. de Jonge Anderson et al. [2024] used
123 reduced-complexity VE models to perform well location and storage capacity assessments in
124 heterogeneous saline aquifers, running thousands of simulations within practical timeframes.
125 Similarly, VE frameworks facilitate the rapid screening of multiple storage sites, robust sensitivity
126 and uncertainty analysis of key parameters affecting plume migration, and probabilistic risk
127 assessment of leakage scenarios [Allen et al., 2018, Tadjer et al., 2021, Pettersson et al., 2022,
128 Anyosa et al., 2024]. For depleted gas reservoirs, where additional uncertainties arise from gas
129 saturation distributions, pressure depletion levels, and CO₂-methane displacement dynamics,
130 the ability to perform comprehensive statistical analysis becomes even more critical.

131 Building upon the foundational VE modeling work for two-phase systems, two important
132 early contributions extended VE concepts to three-phase flow. The first, by Virnovsky et al.
133 [1996], developed a vertically integrated model for gas-oil-water displacement fronts during water-
134 alternating-gas (WAG) operations. Assuming vertical equilibrium and incompressible, immiscible
135 fluids, the authors derived pseudo relative permeability and capillary pressure functions to reduce
136 2D gravity-segregated flow into a 1D formulation. This allowed for analytical exploration of
137 front stability through traveling-wave solutions and was among the earliest works to address
138 three-phase VE dynamics and their implications for vertical sweep efficiency. The second, by
139 Guerrero et al. [2013] and Donat et al. [2014], proposed a one-dimensional three-phase VE model
140 incorporating both buoyancy-driven hyperbolic terms and capillarity-driven parabolic terms.
141 They solved the governing equations using high-resolution Weighted Essentially Non-Oscillatory
142 (WENO) schemes coupled with Implicit–Explicit (IMEX) time-stepping strategies. Their work
143 highlighted the numerical challenges of simulating saturation fronts under VE and provided a
144 robust computational approach. Both studies assumed incompressible fluids and made significant
145 strides in capturing multi-phase dynamics within VE frameworks.

146 In this study, we build upon existing two-phase vertically integrated models by extending
147 them to a three-phase framework. In this approach, CO₂ and methane are treated as two
148 distinct compressible phases, while water is represented as the third, incompressible phase. Our
149 formulation simplifies the problem in two stages: first by reducing a compositional model to a

150 black-oil approximation, and then by collapsing the full 3D representation into a 2D vertically
151 integrated model. This dual simplification enables simulations that are orders of magnitude
152 faster while maintaining reasonable accuracy.

153 **2 Three Phase Vertical Equilibrium Modeling**

154 **2.1 Overview and Assumptions**

155 This study examines CO₂ injection into a depleted gas reservoir system that is vertically confined
156 at both upper and lower boundaries. The reservoir structure consists of one or more gas caps with
157 the remaining volume occupied by brine. Due to depletion, the reservoir pressure is anticipated
158 to be below its initial state. The density of CO₂ is substantially lower than brine but higher
159 than methane across all relevant pressure and temperature conditions. CO₂ exhibits non-ideal
160 behavior, with density and viscosity demonstrating significant variations with pressure and
161 temperature changes. The higher viscosity of CO₂ compared to methane effectively suppresses
162 viscous fingering phenomena and promotes the formation of a stable displacement front. The
163 interaction between CO₂ and methane creates a mixing zone at the front whose characteristics
164 are determined by the competing effects of diffusion and dispersion. At elevated pressures, the
165 density contrast between CO₂ and methane increases (see Figure 8), leading to a narrower
166 mixing zone, particularly under stable stratification conditions. Stable stratification develops
167 when the denser CO₂ layer is positioned beneath the lighter methane layer, preventing convective
168 mixing processes. In contrast, when the denser CO₂ layer overlies lighter methane, gravitational
169 instability develops, substantially accelerating mixing dynamics through convective mixing. In
170 configurations where methane is initially positioned above CO₂, mixing is governed by diffusion.
171 The higher viscosity of CO₂ relative to methane creates a mobility ratio that prevents the
172 development of viscous fingering instabilities [Oldenburg et al., 2001]. Numerical simulations
173 indicate that after CO₂ injection stops, the stored CO₂ continues to sink beneath the overlying
174 methane under density and pressure gradients, forming stratified layers while the mixing zone
175 gradually expands through molecular diffusion [Oldenburg et al., 2001]. Methane is far less dense
176 and viscous than water, so it separates quickly. By contrast, O₂ is less viscous than water but,
177 at higher reservoir pressures, can have a density approaching that of water. It is still typically
178 slightly buoyant and will disengage from the aqueous phase, though with a smaller density
179 contrast than methane [Ghanbari et al., 2020].

180 The conventional black oil modeling framework lacks the capability to define multi-component
181 gas phases. Compositional simulation approaches incorporate equations of state to predict
182 fluid properties and phase interactions under varying pressure and temperature conditions
183 by accounting for the characteristics of individual components. For computational simplicity,
184 this study assumes that the gas plume within the reservoir consists exclusively of methane.
185 The initial compositional model to simulate CO₂ injection into the depleted gas reservoir is
186 developed using the MATLAB Reservoir Simulation Toolbox (MRST) compositional module and
187 subsequently transferred to Jutul Darcy, a high-performance simulator that offers significantly
188 faster computational performance [Lie, 2019, Moyner, 2024]. The model initialization incorporates
189 two-phase saturations comprising an aqueous phase (water) and a gaseous phase (methane),
190 with methane occupying the upper reservoir zones and hydrostatic pressure distribution specified
191 throughout the domain. The system is characterized as a three-phase model encompassing
192 water, oil, and gas phases, where the oil and gas phases represent liquid and vapor phases
193 calculated through equation of state modeling. However, given that both methane and CO₂
194 possess extremely low critical temperatures of -82.59°C and 31.8°C respectively, both components
195 are represented as gas phase constituents in typical reservoir conditions. Consequently, no oil
196 (liquid) phase exists during the simulations, effectively reducing the system to a two-phase
197 water-gas system. To isolate the fundamental CO₂-methane-water displacement mechanisms,

198 water is treated as incompressible with no dissolution effects, and capillary pressure is neglected.
199 These simplifications enable focus on capturing the essential reservoir processes while serving as
200 an initial framework for subsequent detailed modeling efforts. Molecular diffusion and dispersion
201 processes are excluded from this analysis. Although these physical mixing mechanisms are
202 not explicitly incorporated in the model, a mixing zone between fluids can still develop during
203 simulation due to numerical dispersion, which is inherent to the discretization methods employed
204 for solving the governing flow equations. The magnitude of this numerical dispersion depends on
205 factors such as grid resolution, meaning that the observed mixing in simulation results reflects
206 the chosen numerical scheme and may not directly correspond to actual physical mixing processes
207 [Haajizadeh et al., 1999, Shrivastava, 2003, Ghanbari et al., 2018, 2020].

208 The VE model aims to simulate three-dimensional aquifer systems with substantial horizontal
209 extent using two-dimensional representations through the solution of integrated 2D governing
210 equations. This upscaled model formulation relies on the fundamental assumption of VE,
211 requiring the absence of flow perpendicular to the aquifer plane. This assumption must remain
212 valid across the relevant spatial and temporal scales of the system. While VE models can
213 accommodate various physical effects including hysteresis, solubility, and capillary phenomena,
214 the primary objective of this study is to develop a formulation that incorporates CO₂ and
215 methane in a manner consistent with 3D compositional simulations and to evaluate the resulting
216 model performance. Several simplifications are therefore adopted: rock and brine phases are
217 treated as incompressible, no flow occurs through top and bottom boundaries, dissolution
218 and capillary fringe effects are neglected, residual saturations are assumed to be zero, and
219 isothermal conditions are maintained throughout the reservoir. Additionally, mixing phenomena
220 are excluded from the vertical equilibrium model. While this approach ignores the miscible
221 behavior of CO₂ and methane, it preserves the computational benefits of VE modeling while
222 extending its capability to capture key multiphase flow phenomena. We are hence representing
223 the water-gas phase system with water, CO₂ and methane components as a three phase system
224 where each phase represents a component. We show with the help of representative scenarios
225 that due to strong gravity segregation of CO₂ and methane this mixing is a second order effect
226 while first order displacement dynamics, such as the CO₂ plume extent and gas–water contact
227 shape, are captured well with our approach.

228 The ad-core module within MRST provides an object-oriented framework for rapid prototyp-
229 ing of reservoir simulators based on automatic differentiation. This framework facilitates the
230 modification and extension of existing simulation models in MRST or the implementation of new
231 ones. This framework is used to apply the three-phase VE formulation discussed in the following
232 section. The development focuses on an h-formulation system of equations where the primary
233 variables are plume heights rather than saturations, offering a more intuitive representation for
234 VE models.

235 2.2 Governing Equations

236 This section presents the governing equations for a three-phase vertical equilibrium (VE) model
237 designed for multiphase flow in porous media, with particular application to CO₂ storage in
238 depleted gas reservoirs. The model considers a vertically stratified system containing methane,
239 CO₂, and water, arranged according to their densities under the assumption of rapid vertical
240 pressure equilibration. The emphasis is placed on the fundamental assumptions and simplifi-
241 cations inherent in the VE framework, rather than addressing the complexity of reservoir
242 heterogeneity or boundary conditions. Throughout this work, lower-case symbols denote fine-
243 scale, three-dimensional quantities, while the corresponding upper-case symbols (introduced
244 later) represent vertically integrated, VE-scale quantities.

245 The system under consideration involves three immiscible phases flowing through a rigid
246 porous medium under isothermal conditions. The fluid phases are denoted as brine (b), carbon
247 dioxide (c), and methane (m), ordered by density such that $\rho_b > \rho_c > \rho_m$. Each phase occupies

248 a portion of the pore space, and their respective saturations satisfy the constraint.

$$s_b + s_c + s_m = 1 \quad (1)$$

249 The mass conservation principle for each fluid phase $\alpha \in b, c, m$, representing brine, CO₂,
250 and methane respectively, is expressed through the three-dimensional mass balance equation:

$$\frac{\partial}{\partial t} (\rho_\alpha \phi s_\alpha) + \nabla \cdot \rho_\alpha \mathbf{u}_\alpha = \psi_\alpha \quad (2)$$

251 In this formulation, ϕ represents the porosity, s_α denotes the saturation of phase α , \mathbf{u}_α is the
252 corresponding Darcy velocity, and ψ_α accounts for sources or sinks. The velocity field \mathbf{u}_α follows
253 Darcy's law:

$$\mathbf{u}_\alpha = -\frac{k k_{r\alpha}}{\mu_\alpha} (\nabla p_\alpha - \rho_\alpha \mathbf{g}) \quad (3)$$

254 Here, k denotes the absolute permeability, $k_{r\alpha}$ is the relative permeability to phase α , μ_α is
255 the viscosity of phase α , p_α is the pressure of phase α , and \mathbf{g} is the gravitational acceleration
256 vector. In order to derive a vertically integrated flow model, we integrate the mass balance
257 equation (2) over the vertical coordinate, z , from the bottom boundary ζ_B to the top boundary
258 ζ_T :

$$\int_{\zeta_B}^{\zeta_T} \left[\frac{\partial}{\partial t} (\rho_\alpha \phi s_\alpha) + \nabla \cdot (\rho_\alpha \mathbf{u}_\alpha) \right] dz = \int_{\zeta_B}^{\zeta_T} \psi_\alpha dz \quad (4)$$

259 The objective is to express the resulting upscaled equation based on variables that depend
260 solely on the horizontal spatial coordinates (x, y) and time t . Assuming there is no vertical flow
261 through the top and bottom boundaries (i.e., $\mathbf{u}_{\alpha,z} = 0$ at $z = \zeta_B$ and $z = \zeta_T$), and that the
262 boundaries are stationary, the Leibniz rule for differentiation under the integral sign can be
263 applied. This procedure yields the vertically integrated equation:

$$\frac{\partial}{\partial t} \left(\int_{\zeta_B}^{\zeta_T} \rho_\alpha \phi s_\alpha dz \right) + \nabla_{\parallel} \cdot \left(\int_{\zeta_B}^{\zeta_T} \rho_\alpha \mathbf{u}_{\alpha,\parallel} dz \right) = \int_{\zeta_B}^{\zeta_T} \psi_\alpha dz \quad (5)$$

264 where ∇_{\parallel} and $\mathbf{u}_{\alpha,\parallel}$ refer to the horizontal components of the gradient and velocity, respectively.
265 To proceed with the formulation, it is necessary to introduce several quantities that have been
266 integrated over the vertical coordinate. These vertically integrated variables are defined as
267 follows:

$$\Phi := \int_{\zeta_B}^{\zeta_T} \phi dz \quad (6)$$

$$S_\alpha := \frac{1}{\Phi} \int_{\zeta_B}^{\zeta_T} \phi s_\alpha dz \quad (7)$$

$$R_\alpha := \frac{1}{\Phi S_\alpha} \int_{\zeta_B}^{\zeta_T} \rho_\alpha \phi s_\alpha dz \quad (8)$$

$$\Psi_\alpha := \int_{\zeta_B}^{\zeta_T} \psi_\alpha dz \quad (9)$$

$$\mathbf{U}_\alpha := \int_{\zeta_B}^{\zeta_T} \mathbf{u}_{\alpha,\parallel} dz \quad (10)$$

$$\mathbf{F}_\alpha := \int_{\zeta_B}^{\zeta_T} \rho_\alpha \mathbf{u}_{\alpha,\parallel} dz \quad (11)$$

268 Here, Φ denotes the vertically integrated porosity, S_α is the upscaled saturation, and R_α
 269 refers to the upscaled density of phase α . The term \mathbf{U}_α corresponds to the total horizontal
 270 volumetric flux, while \mathbf{F}_α indicates the total horizontal mass flux of phase α across the vertical
 271 column. The term Ψ_α represents the integrated source or sink for phase α over the vertical
 272 domain. Substituting these expressions into equation (5) yields the vertically integrated mass
 273 balance equation:

$$\frac{\partial}{\partial t} (R_\alpha \Phi S_\alpha) + \nabla_{\parallel} \cdot \mathbf{F}_\alpha = \Psi_\alpha \quad (12)$$

274 This vertically integrated formulation accounts for variable density effects, enabling accurate
 275 modeling of density variations throughout the system [Andersen et al., 2015]. To evaluate the
 276 integral of the phase’s lateral mass flux, we incorporate equation (3) into equation (11), yielding:

$$\mathbf{F}_\alpha = - \int_{\zeta_B}^{\zeta_T} \rho_\alpha \lambda_\alpha k_{\parallel} \nabla_{\parallel} p_\alpha dz \quad (13)$$

277 The evaluation of this integral requires the reconstruction of fine-scale quantities based on
 278 coarse scale (upscaled) variables, which can vary depending on the specific modeling approach
 279 and physical context. Certain variables like porosity ϕ and permeability k are predetermined
 280 inputs while others are reconstructed from upscaled quantities under specific assumptions. For
 281 the pressure gradient $\nabla_{\parallel} p_\alpha$ and the density ρ_α , these quantities are expressed relative to reference
 282 values, with the fundamental reference quantity being the reference pressure, termed upscaled
 283 pressure P_α in this formulation. This upscaled pressure represents a two-dimensional field
 284 that varies spatially across the horizontal domain (x_1, x_2) and serves as the primary pressure
 285 variable in the VE formulation. Under the VE assumption, the pressure of each phase p_α varies
 286 hydrostatically in the vertical direction according to:

$$\frac{\partial p_\alpha}{\partial z} = -\rho_\alpha g \quad (14)$$

287 The total hydrostatic pressure change between two vertical depths a and b is determined by
 288 integrating this expression:

$$\Delta p_\alpha = - \int_a^b \rho_\alpha g dz \quad (15)$$

289 This relationship allows the vertical pressure profile to be reconstructed from an upscaled
 290 phase pressure, typically taken at either the bottom or top of the column. Denoting the phase-
 291 specific pressure at the bottom as $P_\alpha(x_1, x_2, t)$, the vertical pressure distribution for each phase
 292 under equilibrium conditions is written as:

$$p_\alpha(x_1, x_2, z, t) = P_\alpha(x_1, x_2, t) - g \int_{\zeta_B}^z \rho_\alpha dz' \quad (16)$$

293 To proceed with the formulation, we must define the phase densities. In our case, brine is
 294 assumed to be incompressible, while the densities of CO₂ and methane vary with pressure under
 295 the assumption of constant temperature. We capture this relationship by fitting an equation
 296 to equation-of-state (EoS) data, as described in A. A key challenge arises because we are only
 297 solving for the VE reference (bottom) pressure rather than for the entire column, and we need
 298 to provide the density values across the interval. Consequently, we must incorporate a density
 299 profile that depends on the hydrostatic pressure distribution—which itself depends on the density
 300 at other points. This interdependence introduces a nonlocal effect. The most direct approach
 301 would involve numerically reconstructing the full vertical density profile at every timestep and
 302 integrating across the column, but this method is computationally expensive.

To avoid this computational cost, a Taylor series expansion is employed that allows rep-
 resentation of a function locally in terms of its value and derivatives at a reference point. In

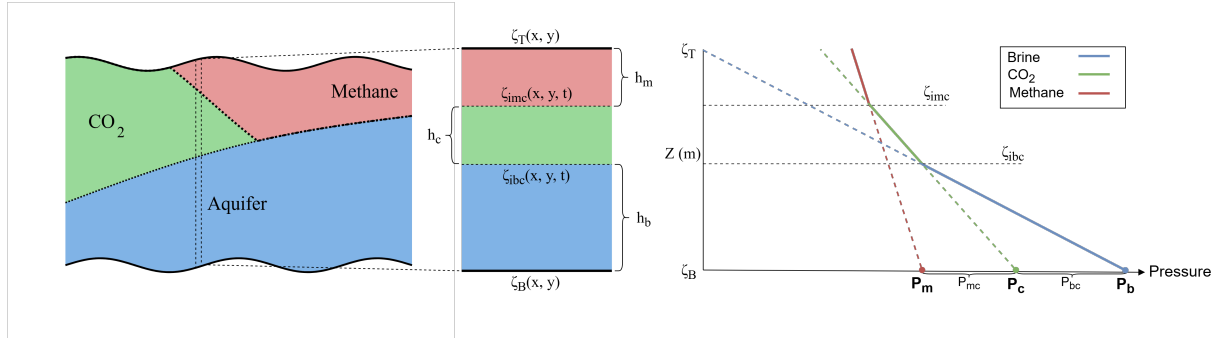


Figure 1: A schematic of phase interfaces and plume heights

this context, the expansion is applied to the density functions of the compressible phases to approximate their density profile over their respective phase fluid columns. By integrating this approximated density function over each fluid column, an “upscaled” density equation is obtained that corresponds to the total mass of that phase in the column. We limit the Taylor series to second-order terms and expand around a reference pressure (i.e., the upscaled pressure), which leads to the following density equation:

$$\rho_\alpha(p) \approx \rho_\alpha(p_{ref}) - \frac{\rho'_\alpha(p_{ref})}{1!} \rho_\alpha(p_{ref}) g [z - \zeta_{ref}] + \frac{\rho''_\alpha(p_{ref})}{2!} (\rho_\alpha(p_{ref}) g [z - \zeta_{ref}])^2 \quad (17)$$

303 This expression is valid for any reference point situated within the reservoir’s height. In this
 304 study, we chose the bottom of the reservoir as the reference point, meaning the phase pressures
 305 at this depth are taken as the reference pressure. A similar Taylor series approach is adopted for
 306 representing viscosity. For flux calculations, the formulation is simplified by retaining only the
 307 zeroth-order terms of both density and viscosity, ignoring higher-order terms and evaluating
 308 them at a single reference pressure:

$$\rho_\alpha(p) \approx \rho_\alpha(p_{ref}), \quad \mu_\alpha(p) \approx \mu_\alpha(p_{ref}) \quad (18)$$

309 This approximation implies that density and viscosity variations along the vertical coordinate
 310 are negligible, enabling these terms to be factored out of vertical integrals.

311 To efficiently address the system of equations, standard practice involves selecting and solving
 312 explicitly for a single-phase pressure, with the pressures of other phases expressed relative to
 313 this reference through pressure differences. The vertical domain is divided into distinct regions
 314 by phase interfaces located at $\zeta_{i\alpha\beta}$, where adjacent phases α and β meet. At these interfaces,
 315 the pressure difference between two adjacent phases is defined by subtracting the hydrostatic
 316 contribution from each other:

$$p_{\alpha\beta} = P_{\alpha\beta} - g \int_{\zeta_B}^{\zeta_{i\alpha\beta}} (\rho_\alpha - \rho_\beta) dz \quad (19)$$

317 When fine-scale effects like capillary pressure are neglected, the pressure difference between
 318 each pair of phases at the interfaces becomes zero. This simplification reduces the equations to:

$$P_{\alpha\beta} = g \int_{\zeta_B}^{\zeta_{i\alpha\beta}} (\rho_\alpha - \rho_\beta) dz \quad (20)$$

319 Incorporating the density approximation eq (18) into the upscaled pressure difference equa-
 320 tions yields:

$$P_{\alpha\beta} = (\rho_\alpha(P_\alpha) - \rho_\beta(P_\beta)) g (\zeta_{i\alpha\beta} - \zeta_B) \quad (21)$$

321 Here, P_β refers to the phase β pressure at the bottom, and the subscripts α and β represent
 322 any two adjacent phases in the multi-phase system. However, this choice introduces a circular

323 dependency: the upscaled pressure difference needed to calculate the phase β pressure from
 324 the phase α pressure depends on the phase β density, while the phase β density itself requires
 325 knowledge of the phase β pressure. Solving this implicit coupling directly would demand iterative
 326 reconstruction of the phase β pressure at every timestep, which is computationally expensive.
 327 To avoid this computational complexity, we expand $\rho_\beta(P_\beta)$:

$$\begin{aligned}\rho_\beta(P_\beta) &= \rho_\beta(P_\alpha + P_{\alpha\beta}) \\ &\approx \rho_\beta(P_\alpha) + \left. \frac{\partial \rho_\beta}{\partial P} \right|_{P_\alpha} \cdot P_{\alpha\beta}\end{aligned}\quad (22)$$

328 In our formulation, CO₂ pressure is the primary unknown variable we solve for (phase α),
 329 with water and methane as phase β . Since water is incompressible and methane is weakly
 330 compressible, the density derivative $\left. \frac{\partial \rho_\beta}{\partial P} \right|_{P_\alpha}$ becomes zero or negligible. Additionally, pressure
 331 differences are small relative to absolute pressures in the system. These conditions allow us to
 332 evaluate phase β density at the phase α pressure (P_α) rather than the phase β pressure (P_β),
 333 which eliminates the circular dependency and simplifies the pressure difference equations to
 334 depend only on phase α pressure. Additionally, the interface depths are subsequently expressed
 335 in terms of phase thicknesses as follows:

$$\begin{aligned}\text{brine} : \quad h_b &\equiv \zeta_{ibc} - \zeta_B \\ \text{carbon dioxide} : \quad h_c &\equiv \zeta_{imc} - \zeta_{ibc} \equiv H - h_m - h_b \\ \text{methane} : \quad h_m &\equiv \zeta_T - \zeta_{imc}\end{aligned}\quad (23)$$

336 Where $H = \zeta_T - \zeta_B$. Here, the CO₂ phase height is expressed as a function of the brine and
 337 methane heights, thereby reducing the number of independent unknowns, in a manner similar to
 338 three-phase black-oil models where saturations are the primary variables. These changes yield
 339 phase-specific equations for CO₂-brine and CO₂-methane as follows:

$$P_{bc} = (\rho_b - \rho_c(P_c)) g h_b \quad (24)$$

$$P_{mc} = (\rho_c(P_c) - \rho_m(P_c)) g (H - h_g) \quad (25)$$

340 Based on the new density and phase height expressions, we reformulate the pressure equations
 341 and compute the lateral pressure gradients for each phase. Assuming an incompressible brine
 342 and CO₂ and methane densities independent of the vertical coordinate, along with negligible
 343 lateral variations in density and gravitational effects, we obtain the following phase-specific
 344 expressions for $\nabla_{\parallel} p_\alpha$:

$$\nabla_{\parallel} p_\alpha = \nabla P_\alpha + \rho_\alpha(P_\alpha) g \nabla \zeta_B \quad (26)$$

346 Note that the final pressure gradients are not a function of z and are taken out of the integral
 347 in equation (13). We now define other vertically integrated variables as follows:

$$K := \int_{\zeta_B}^{\zeta_T} k_{\parallel} dz \quad (27)$$

$$\Lambda_\alpha := \frac{1}{K} \int_{\zeta_B}^{\zeta_T} \lambda_\alpha k_{\parallel} dz \quad (28)$$

$$\tilde{R}_\alpha := \frac{1}{K \Lambda_\alpha} \int_{\zeta_B}^{\zeta_T} \rho_\alpha \lambda_\alpha k_{\parallel} dz \quad (29)$$

348 Where K and Λ_α are vertically integrated permeability and mobility terms, respectively. The
 349 variable \tilde{R}_α is introduced to account for density effects in the integrated flux term. Specifically,
 350 \tilde{R}_α is defined as the upscaled phase density weighted by mobility and permeability. When
 351 assuming either incompressible fluids or compressible fluids with no dependence on the vertical
 352 coordinate (i.e., equation (18)), the density is taken outside the integral, resulting in:

$$\tilde{R}_\alpha = \begin{cases} \rho_\alpha, & \alpha = b, \\ \rho_\alpha(P_{ref}), & \alpha \in \{c, m\}. \end{cases} \quad (30)$$

353 Having established the vertically integrated density \tilde{R}_α , we now turn to the pressure gradient
 354 term in Darcy's equation (3). In the special case of a fully homogeneous reservoir ($k_{\parallel} = k = \text{const}$),
 355 a sharp-interface model with no residual saturations (λ_α takes only saturation values of 0 or 1),
 356 the constant permeability moves out of the integrals. This permits analytical integration and
 357 allows Λ_α to be explicitly defined for each phase:

$$\Lambda_\alpha = \frac{k}{kH} \int_{\zeta_B}^{\zeta_T} \lambda_\alpha dz = \lambda_\alpha(1) \frac{h_\alpha}{H}. \quad (31)$$

358 The flow interaction between CO₂ and methane is modeled using a shared relative permeability
 359 curve for both components, consistent with the conventional compositional approach in which
 360 they are treated as a single phase. Consequently, the endpoint mobilities for the two components
 361 share the same relative permeability value at full saturation, meaning $k_{rm}(1) = k_{rc}(1)$. As given
 362 in equation (18), the viscosity terms in λ_α do not vary with the vertical coordinate and can
 363 therefore be pulled out of the integral.

364 The final upscaled mass flux terms for each phase are written using the coarse-scale perme-
 365 ability and mobilities as:

$$\mathbf{F}_\alpha = -\tilde{R}_\alpha \Lambda_\alpha K (\nabla P_\alpha + \rho_\alpha(P_\alpha) g \nabla \zeta_B). \quad (32)$$

366 Returning to the upscaled mass accumulation term in equation (8), for a homogeneous
 367 reservoir and given that saturation is either zero or one, we can restrict the integration domain
 368 for each phase to the vertical interval where its saturation is one. This simplifies equation (8) to:

$$R_\alpha \Phi S_\alpha = \phi \int_{\zeta_a}^{\zeta_b} \rho_\alpha dz, \quad \{a, b\} \in \{B, ibc, imc, T\} \quad (33)$$

369 Where ζ_a to ζ_b denotes the vertical region occupied entirely by the phase α . For brine, which
 370 is incompressible, density can be taken outside the integral, yielding a simplified expression.
 371 For CO₂ and methane density functions, however, rather than neglecting higher-order terms,
 372 we retain them and evaluate the vertical integral of the density function from equation (17),
 373 resulting in:

$$R_\alpha = \rho_\alpha(p_a) [\zeta_b - \zeta_a] - \frac{\rho'_\alpha(p_a)}{1!} (\rho_\alpha(p_a) g) \frac{[\zeta_b - \zeta_a]^2}{2} + \frac{\rho''_\alpha(p_a)}{2!} (\rho_\alpha(p_a) g)^2 \frac{[\zeta_b - \zeta_a]^3}{3}, \quad \{\alpha\} \in \{c, m\} \quad (34)$$

374 This expression is then used in the mass accumulation term for CO₂ and methane, where
 375 the reference pressure matches that used in the upscaled phase density of the flux term. The
 376 final vertically integrated flow equations become the following:

$$-\Phi \frac{\partial(R_\alpha S_\alpha)}{\partial t} + \nabla \cdot \mathbf{F}_\alpha = \Psi_\alpha \quad (35)$$

377 The vertically integrated equations derived above were implemented in the MATLAB
 378 Reservoir Simulation Toolbox (MRST) using its Automatic Differentiation framework [Lie and

379 Møyner, 2021]. The approach uses plume heights as the primary variables and calculates phase
380 fluxes based on vertically averaged mobilities and hydrostatic pressure gradients, consistent
381 with VE assumptions. This setup retains the analytical structure of the VE formulation while
382 utilizing MRST’s ADI capabilities for residual construction, Jacobian computation, and fully
383 implicit time integration, ensuring both robustness and scalability.

384 **3 Results and Discussion**

385 This section shows the results from three case studies using the three-phase VE model developed
386 in this work, and compares them to compositional simulations. The first case uses a flat, layered
387 synthetic reservoir to benchmark the VE model against compositional simulations in an idealised
388 geometry. The second looks at a dual-anticline structure to assess grid sensitivity and structural
389 trapping behavior. The third applies the model to the real-world Hugin Formation East to
390 evaluate its performance in a geologically realistic field setting. As described earlier, the initial
391 compositional models were built with the MRST compositional module, then transferred and
392 executed in Jutul Darcy. Simulations were carried out either on a local workstation with an Intel
393 Core i9-14900K processor or on the DMOG HPC cluster. Some simulations also used MPI-based
394 parallel computing to speed up the runtimes. Brine properties are treated as incompressible in
395 both the compositional and VE models, using constant values of 1000 kg m^{-3} for density and 1 cP
396 for viscosity. In the VE model, methane and CO_2 are treated as compressible fluids, with their
397 density and viscosity defined by pressure-dependent correlations, as outlined in Section 2. The
398 compositional model uses an equation of state (EoS) to compute the thermophysical properties
399 of methane and CO_2 .

400 **3.1 Case 1 — Flat-Layered Gas–Brine Benchmark**

401 The first case study features a simplified flat-layered synthetic reservoir model, designed as a
402 benchmark scenario to study basic flow behavior in compositional simulations. The model has
403 a uniform structure with no topographic variation and spans 10 kilometers in the horizontal
404 direction with a constant vertical thickness of 50 meters. The domain is initialized with the upper
405 half of the reservoir saturated with methane, while the lower half contains brine, representing a
406 stratified two-phase system. The reservoir pressure is set to 150 bar at the gas–water interface,
407 with a hydrostatic pressure distribution applied throughout the domain. The porosity is set
408 uniformly at 20%, and the permeability is isotropic, with values of 100 mD. The reservoir is
409 discretized into a structured grid with 1000 horizontal cells ($dx = 10 \text{ m}$) and 100 vertical layers
410 ($dz = 0.5 \text{ m}$), yielding a total of 100,000 grid cells. Injection is performed from a well at the
411 left side at a constant rate of 2000 kg/day for a period of 30 years, while the right boundary
412 maintains constant hydrostatic pressure.

413 Figure 2 compares the fine-grid compositional simulation to the three-phase VE model for
414 the benchmark scenario. The compositional model shows a more diffuse and vertically mixed
415 transition zone between CO_2 and methane, particularly farther from the injection well, whereas
416 the VE model effectively approximates the leading front of the CO_2 plume as it displaces the
417 methane gas at the top of the reservoir. Agreement is especially strong at the brine– CO_2
418 interface, where the VE model closely follows the lower boundary of the migrating plume. These
419 results confirm that, despite its simplified assumptions, the VE model captures the key large-scale
420 displacement and plume geometry. Its sharp interface approximation provides a robust match
421 to the dominant flow behavior observed in the compositional simulation.

422 A key observation in this scenario is that, despite CO_2 being co-injected into both brine- and
423 methane-saturated zones, the majority of the CO_2 plume preferentially migrates upward into
424 the methane-rich region, while its advancement within the brine zone is comparatively slower.
425 This response is governed primarily by fluid mobility contrasts in a pressure-driven system, with

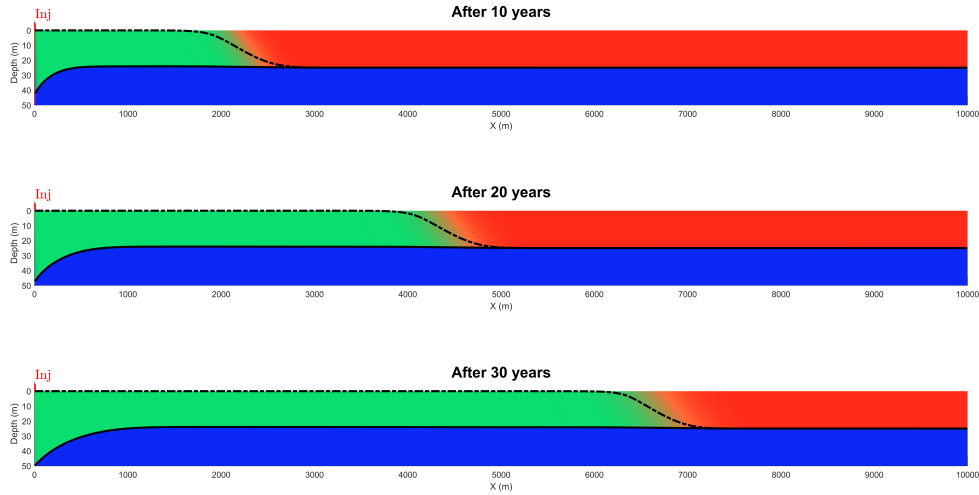


Figure 2: Compositional simulation (colored fields) versus VE model predictions (black lines) for Case 1. The VE model approximates the CO_2 (green) plume’s migration into methane (red) and along the brine (blue) interface at 10, 20, and 30 years.

426 gravity exerting an influence through gravitational segregation. In particular, CO_2 displacing
 427 methane is more favorable than CO_2 displacing water because the CO_2 –methane mobility ratio
 428 is closer to unity than the CO_2 –brine mobility ratio. This setup serves as a reference to validate
 429 fluid behavior and mobility under simplified conditions before moving on to more geologically
 430 complex cases.

431 3.2 Case 2 — Dual-Anticline Grid-Sensitivity Benchmark

432 In the second scenario, a two-dimensional reservoir with a sinuous geometry and two anticlines
 433 was used to examine CO_2 plume migration under geologically realistic conditions. The initial
 434 gas–brine configuration, with a 30-meter-thick gas cap in the left anticline and the remainder of
 435 the reservoir saturated with water, is shown in Figure 3a, while the subdivision of the domain
 436 into two indexed anticline compartments used for subsequent analysis is shown in Figure 3b.
 437 CO_2 is injected at a constant rate of 25 t/year for 50 years through a well located at the left
 438 boundary. A constant hydrostatic pressure was maintained at the right boundary, and all other
 439 boundaries were treated as no-flow. The simulation continued for 2000 years after injection
 440 ceased. The initial pressure at the deepest point in the reservoir was set to 200 bar, and the
 441 resulting hydrostatic pressure field is illustrated in Figure 3c, with pressures across the domain
 442 calculated based on local fluid saturations. The model domain extends 5 km laterally, 50 m
 443 vertically, and 1 m in width, with uniform rock properties defined by a porosity of 20% and a
 444 permeability of 10 mD.

445 Compositional simulations were performed on a refined grid to provide a converged reference
 446 solution for comparison with the VE model. The comparison focuses on the predicted redistri-
 447 bution of CO_2 and methane between the two anticlines, as illustrated by the time evolution
 448 of phase distributions in the bottom panels of Figure 3, where the compositional results are
 449 shown alongside the VE model. To further examine the behaviour in each structure, two indexed
 450 regions in the anticlines were tracked over time (see Figure 3b), and the corresponding evolution
 451 of CO_2 and methane mass in each compartment is summarized in Figure 4.

452 The mass balance evolution in each anticline, shown in Figure 3 and Figure 4, is used to
 453 compare the VE model against the compositional reference solution. The comparison focuses on

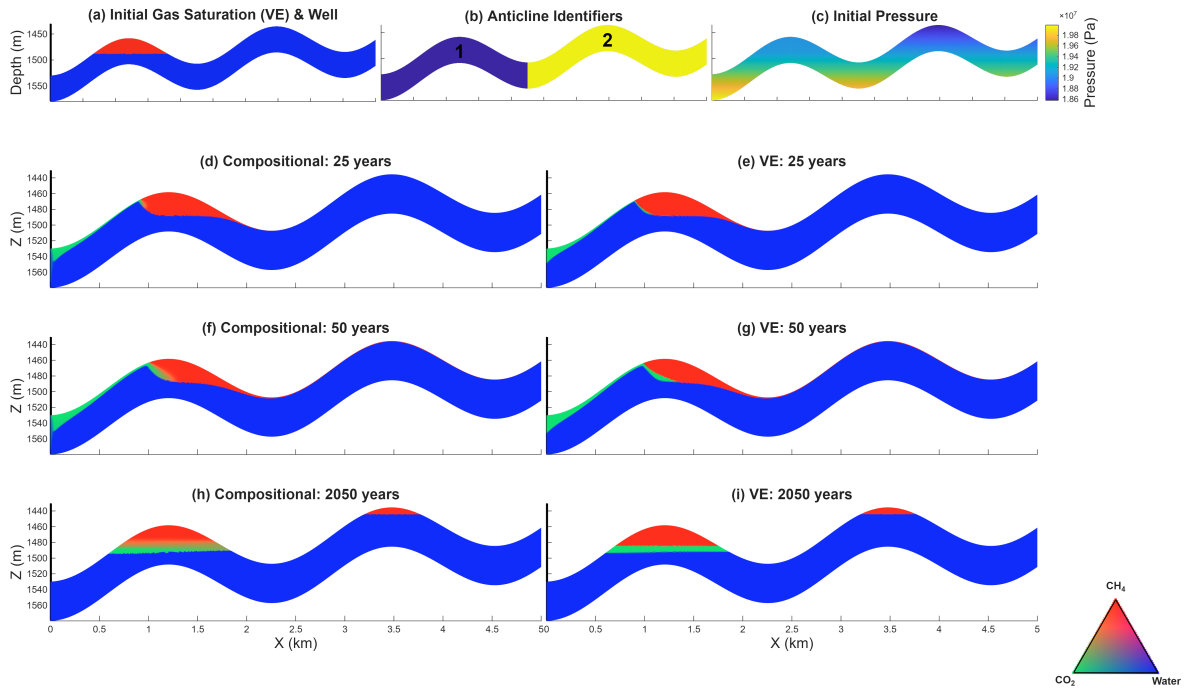


Figure 3: Structural reservoir model and temporal evolution of gas migration. Top row: (a) Initial gas saturation (methane shown in red) and injection well location; (b) Domain segmentation highlighting individual anticline structures used for mass balance tracking; (c) Initial hydrostatic pressure distribution (Pa) across the 5 km domain. Rows 2–4: Comparison of gas plume migration between the Compositional model (left column: d, f, h) and the VE model (right column: e, g, i) at 25, 50, and 2050 years. The snapshots illustrate the displacement of the initial methane (red) by the injected CO₂ (green) and the subsequent structural trapping within the anticline formations.

454 the redistribution of CO₂ and methane between the two structural compartments and on the
 455 corresponding component inventories over time. Overall, the VE results reproduce the main
 456 trends of the compositional model, including the partitioning of mass between the anticlines and
 457 its temporal evolution. Since the compositional model is taken here as the reference solution,
 458 the purpose of this comparison is to assess how well the VE formulation captures the large scale
 459 migration behaviour relevant to this case. It should also be noted that the compositional model
 460 does not include molecular diffusion or hydrodynamic dispersion.

461 3.3 Case 3 — Field-scale demonstration: Hugin Formation East

462 The third study uses the publicly available *Hugin Formation East* dataset from the CO₂ Storage
 463 Atlas of the Norwegian Continental Shelf [Bjørnstad et al., 2017]. The Hugin Formation, located
 464 in the South Viking Graben of the North Sea, comprises Middle Jurassic shallow-marine and
 465 marginal-marine sandstones deposited during a regional transgression. Here, we use the averaged
 466 formation values across the whole formation ($\phi = 12.45\%$, $k = 500$ mD). The simulation grid is
 467 a corner-point mesh that honours the complex geometry: 2264×20 cells (horizontal \times vertical)
 468 for a total of 45 280 active cells, covering $\sim 2.26 \times 10^3$ km² with layer thicknesses ranging from
 469 5.8 to 106.4 m.

470 The model was initialized with 15 % methane gas and 85 % brine in every cell. A preliminary
 471 run is performed so that pressure and saturations relax to hydrostatic equilibrium; this state
 472 becomes the initial condition for the main study. A single injector, placed near the structural

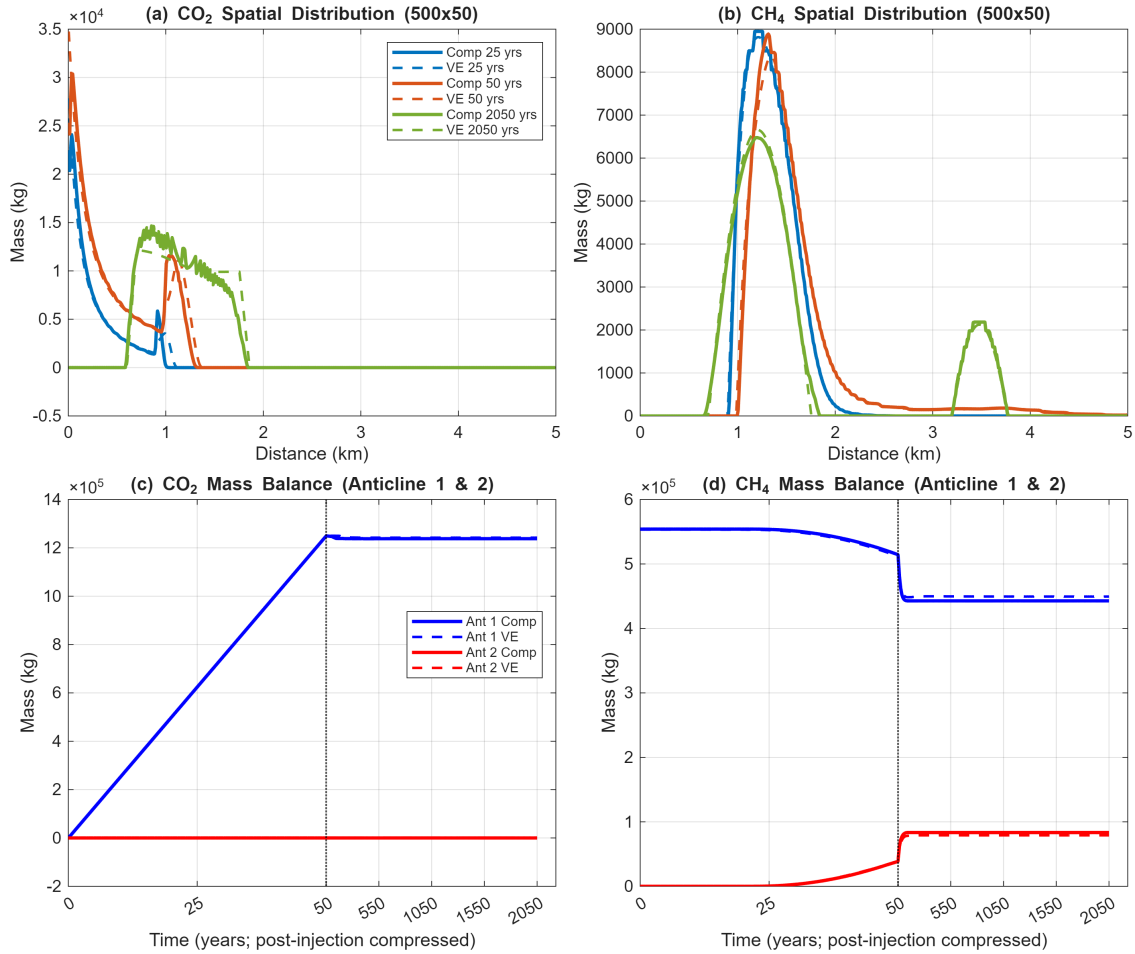


Figure 4: Spatial distribution and mass balance analysis for CO₂ and methane. (a) CO₂ spatial distribution along the domain at 25, 50, and 2050 years. (b) Methane spatial distribution showing the migration and attenuation of the gas plume over time. (c) Cumulative CO₂ mass balance within Anticline 1 and Anticline 2, showing primary containment in Anticline 1. (d) Methane mass balance illustrating the secondary migration from Anticline 1 to Anticline 2. Solid lines indicate the full compositional model (Comp), while dashed lines represent the Vertical Equilibrium (VE) approximation.

473 center, injects 2.5 Mt yr^{-1} of CO₂ for 50 years. After shut-in, the simulation continues for 1 000
 474 years to capture the post-injection redistribution and trapping processes. Figure 6 shows a top
 475 view of the compositional simulations compared to the VE model after 10, 50 and 1050 years.

476 10 years. Both models predict nearly identical plume footprints. The VE solution appears
 477 smoother because it integrates over the vertical direction and is therefore insensitive to vertical
 478 resolution or the precise shape of the relative-permeability curves.

479 50 years (end of injection). The plume has migrated downdip beneath the pre-existing methane
 480 cap. Crucially, both models place the leading edge at virtually the same x - y location, confirming
 481 that the VE model captures the dominant buoyancy- and mobility-controlled dynamics.

482 1050 years (end of migration). CO₂ primarily occupies the smaller anticlines close to the injection
 483 site, displacing the methane that originally resided there into larger and shallower structural
 484 traps. The VE model captures the overall redistribution pattern well but underpredicts methane
 485 displacement in smaller anticlines, compared to the compositional model. This discrepancy
 486 arises in part from numerical dispersion in the compositional model, where coarse grid resolution

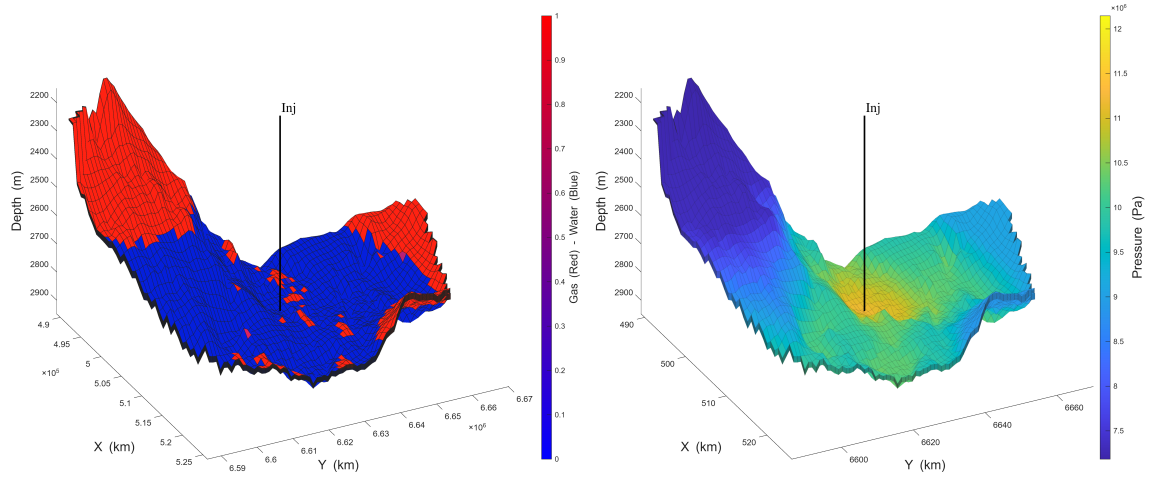


Figure 5: Case 3, Initial saturation and pressure distribution shown from two viewing angles.

487 leads to exaggerated mixing and overestimation of methane movement. However, the VE model
 488 also contributes to this difference by excluding mixing processes altogether, which limits its
 489 ability to fully represent gas displacement dynamics. The transition zone between CO₂ and
 490 methane within the larger gas caps is similarly influenced by both numerical dispersion in the
 491 compositional model and the absence of mixing in the VE formulation.

492 Another key difference lies in the amount of trapped gas predicted by the two models. The
 493 VE model uses an analytical approach to estimate vertical saturation, making it independent of
 494 vertical grid resolution. In contrast, the 3D compositional model relies on explicit gridding, which
 495 can lead to the uppermost cells in smaller anticlines being fully saturated with gas. As a result,
 496 the VE model tends to predict a thinner gas column in these regions. This discrepancy, therefore,
 497 is due to differences in vertical resolution and the level of detail in the grid discretization.

498 Overall, the VE model reproduces the dominant features of plume evolution, structural
 499 trapping, and long-term redistribution while running orders of magnitude faster than the full
 500 compositional calculation, as quantified by the comparison of simulation times in Table 1. This
 501 makes VE modelling a powerful tool for rapid field-scale screening and optimisation of prospective
 502 CO₂ storage sites, particularly where millennial-scale performance must be evaluated across
 503 many geological realizations.

Table 1: Comparison of Simulation Times for Compositional and VE simulations

Scenario	Compositional (s)	VE (s)
Case 1	15228	36
Case 2	65952	42
Case 3	72360	330

504 3.4 Discussion

505 The present study extends the well-established VE modeling framework to account for flow
 506 involving CO₂, methane, and brine in depleted gas reservoirs. While previous applications of
 507 VE models have demonstrated their utility in simulating the large-scale migration of CO₂ in
 508 two-phase (i.e., CO₂-brine) systems with significant computational savings (Gasda et al., 2009;
 509 Nordbotten and Celia, 2011; Court et al., 2012), their application to depleted gas fields has not
 510 previously been explored.

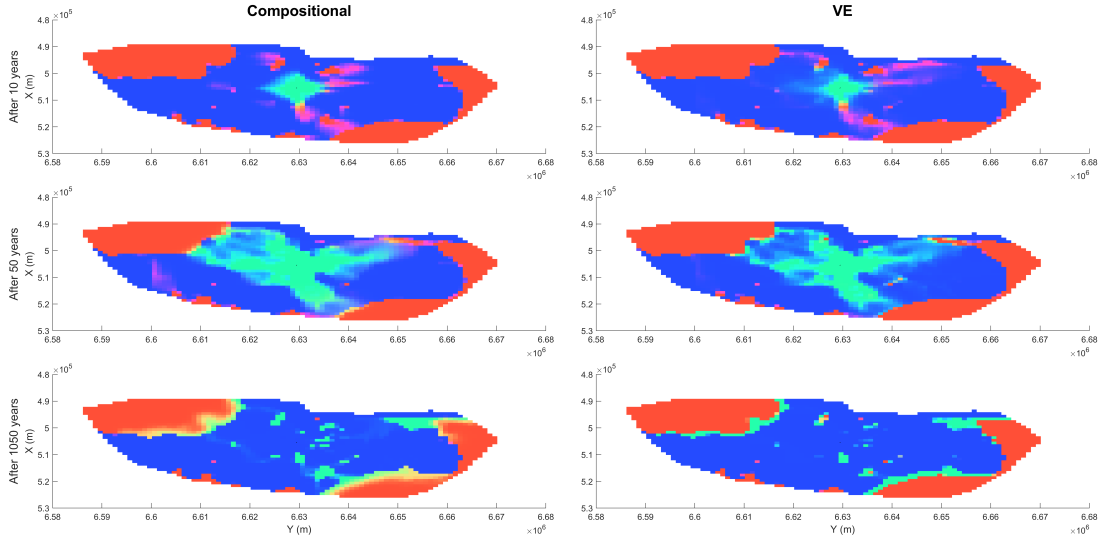


Figure 6: Case 3, Top-view comparison of CO₂ and methane plume migration after 10, 50, and 1050 years using compositional (left column) and VE (right column) models. The spatial extent of the plume is shown in the XY plane.

511 Across all three case studies, the three-phase VE formulation reproduced the large-scale
 512 behavior seen in compositional simulations. (i) *Flat, layered benchmark*: the VE model accurately
 513 captured the migration of CO₂ into the methane layer and the shape of the CO₂-brine interface.
 514 (ii) *Dual anticlines*: the VE model compared well with the compositional simulations, reproducing
 515 the large-scale plume geometry and inter-anticline mass redistribution; a supplementary outcome
 516 of this test was that the comparison also revealed a strong sensitivity of compositional results
 517 to vertical grid resolution. (iii) *Field scale (Hugin Formation)*: the VE model successfully
 518 replicated the plume migration, structural trapping, and long-term redistribution predicted by
 519 the compositional model, confirming its applicability to realistic geological settings.

520 Across all three cases, certain model limitations became apparent, primarily stemming from
 521 the fundamental assumptions of the VE framework. The most significant limitation is the model's
 522 current inability to simulate mixing between CO₂ and methane. The current formulation treats
 523 CO₂ and methane as immiscible phases with a sharp interface. Consequently, the model cannot
 524 replicate phenomena driven by convective mixing, which may be important in scenarios involving
 525 direct injection into methane-saturated zones or in highly heterogeneous formations. These
 526 limitations are largely due to the core assumptions of the VE method itself, rather than just the
 527 fact that it doesn't model mixing. This simplification, while enabling computational speedup,
 528 resulted in some discrepancies in predicted volumes of displaced CO₂ and methane within
 529 structural traps, particularly when compared to compositional simulations. Additionally, the
 530 current formulation excludes other physical mechanisms known to enhance long-term trapping,
 531 namely the dissolution of CO₂ into brine and capillary fringe effects, though these mechanisms
 532 could be incorporated using established methods from two-phase VE systems [Andersen, 2017,
 533 Nilsen et al., 2016b].

534 4 Conclusion

535 This study introduces and evaluates a three-phase VE modeling framework for simulation of CO₂
 536 migration in depleted gas reservoirs, explicitly accounting for the presence of methane. The VE
 537 formulation simplifies the compositional model into a black-oil approximation and subsequently

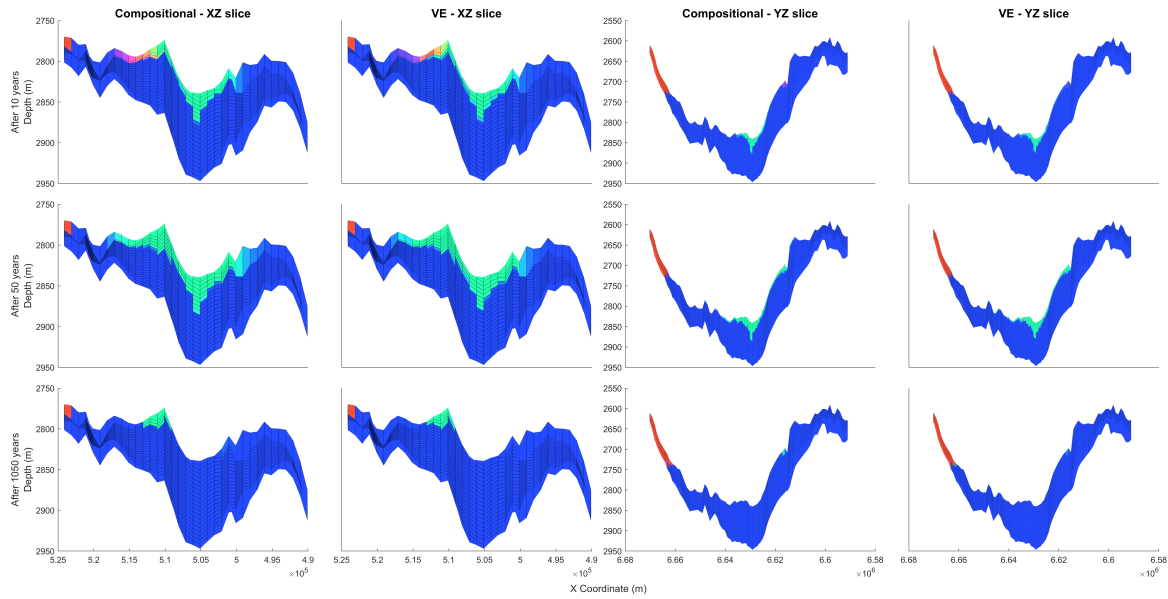


Figure 7: Case 3, Comparison of CO₂ and methane plume evolution at three time steps (10, 50, and 1050 years) for compositional and vertical equilibrium (VE) models. XZ and YZ 2D cross-sections are shown for each case.

538 collapses the spatial domain into two dimensions with significant computational speedup.

539 Benchmarking across idealized and field-scale configurations shows that the model captures
 540 the key gravity-driven plume shape, lateral migration pathways, and locations of structural
 541 trapping that are most relevant for reservoir- to basin-scale assessment. Because vertical
 542 profiles are handled analytically, the formulation is largely insensitive to vertical grid refinement
 543 while coarse-grid compositional simulations are susceptible to numerical dispersion and can
 544 misrepresent the amount of fluid spilling across anticlines. Quantitatively, differences are most
 545 apparent near sharp contacts and in zones where small-scale mixing controls phase volumes, but
 546 the regional patterns and time scales of migration remain well reproduced.

547 Despite known limitations, the VE model delivers substantial computational gains, typically
 548 on the order of 10^2 – 10^3 relative to compositional models, cutting runtimes from hours or days
 549 to minutes or seconds and enabling simulations over long timeframes and large domains. This
 550 dramatic speed-up enables ensemble-centric workflows that would otherwise be impractical:
 551 rapid site screening over large geographic extents (especially valuable in early CCS project
 552 stages), systematic sensitivity studies and assessment of injection strategies, optimization under
 553 operational constraints, and workflows requiring several runs such as uncertainty quantification
 554 and history matching. For the early stages of CCS project development, where rapid screening of
 555 potential sites and assessment of various injection strategies are critical, such a tool is invaluable.
 556 While this study focused on CO₂ injection into depleted gas reservoirs, the framework is adaptable
 557 to other subsurface applications characterized by gravity segregation and extensive lateral scales,
 558 including energy storage, CO₂-enhanced gas recovery, and water-alternating-gas processes.

559 Open Research Section

560 The data associated with this manuscript will be made publicly available upon publication of
 561 the journal article.

562 Conflict of Interest disclosure

563 To the best of the authors' knowledge, there are no conflicts of interest associated with this
564 work.

565 Acknowledgments

566 Saeid Telvari acknowledges the support of a James Watt Scholarship from Heriot-Watt University.
567 This work is part of the MuPSI project (Multiscale Pressure-Stress Impacts on fault integrity for
568 multi-site regional CO₂ storage) which operates under the Clean Energy Transition Partnership
569 (CETP).

570 Declaration of Generative AI Use

571 AI language models were used to assist with aspects of manuscript preparation. All content was
572 reviewed, verified, and approved by the authors, who take full responsibility for the manuscript.

573 A Thermophysical Property Modeling of CO₂ and Methane

574 The density and viscosity properties of CO₂ and methane are determined through flash calcula-
575 tions using the equation of state across a range of pressures at 60°C. These computational results
576 are subsequently used to develop fitted equations describing the pressure-dependent variations
577 in density and viscosity for each component. The fitting procedure employs Fourier-type series
578 equations with 3 to 8 terms, depending on the specific dataset characteristics. The accuracy of
579 the fitted equations is quantified using root mean squared error analysis, as shown in Table 2.
580 Notably, the errors associated with CO₂ are larger due to its more non-ideal behaviour compared
581 to methane. The fitting equation takes the form:

$$f(p) = a_0 + \sum_{n=1}^8 [a_n \cos(n\omega p) + b_n \sin(n\omega p)] \quad (36)$$

582 Here, $f(p)$ represents the fitted property (density or viscosity) as a function of pressure p , a_0 ,
583 a_n , and b_n are fitting coefficients, ω is a frequency parameter, and n is the number of harmonic
584 terms used, determined for each specific fluid and property being modeled.

Table 2: RMSE Errors between Fitted Equations and EoS Data

Property	CO ₂	CH ₄
Density	0.2137	4.1728e-05
Viscosity	2.23358e-08	2.4823e-10

585 References

- 586 M Ahmadinia, S M Shariatipour, O Andersen, and M Sadri. Benchmarking of vertically
587 integrated models for the study of the impact of caprock morphology on CO₂
588 migration. *International Journal of Greenhouse Gas Control*, 90, 2019. ISSN 1750-5836. doi:
589 10.1016/j.ijggc.2019.102802. URL [GotoISI://WOS:000495026000009](https://www.sciencedirect.com/science/article/pii/S1750583619300009).
- 590 A. Al-Hashami, S. R. Ren, and B. Tohidi. CO₂ Injection for Enhanced Gas Recovery and
591 Geo-Storage: Reservoir Simulation and Economics. 6 2005. doi: 10.2118/94129-MS. URL
592 <https://dx.doi.org/10.2118/94129-MS>.

Table 3: Fitted Fourier coefficients and frequency parameter (ω) for pressure-dependent property correlations

Coeff	ρ_c	ρ_m	μ_c	μ_m
a_0	4.647e+02	6.811e+01	4.717e-05	2.058e-05
a_1	-3.783e+02	-6.191e+01	-1.989e-05	-9.762e-06
b_1	-1.631e+02	1.372e+02	-2.211e-05	1.016e-06
a_2	-1.142e+02	-7.962e+00	-8.102e-06	1.302e-06
b_2	1.674e+01	-2.807e+01	-2.916e-06	7.019e-07
a_3	2.506e+00	-1.246e+00	-3.038e-06	6.118e-08
b_3	5.676e+01	2.240e+01	3.585e-06	-4.160e-07
a_4	2.021e+01	4.839e+00	-5.284e-07	–
b_4	2.251e+01	-7.902e+00	2.918e-06	–
a_5	6.303e+00	-1.827e+00	5.821e-07	–
b_5	-3.976e+00	2.764e-01	8.952e-07	–
a_6	-9.955e-01	–	5.955e-07	–
b_6	-4.553e+00	–	9.503e-09	–
a_7	-2.635e-01	–	2.104e-07	–
b_7	7.068e-01	–	-4.759e-08	–
a_8	4.358e-01	–	–	–
b_8	1.176e+00	–	–	–
ω	1.377e-07	4.909e-08	1.398e-07	6.545e-08

593 Rebecca Allen, Halvor M. Nilsen, Knut Andreas Lie, Olav Møyner, and Odd Andersen. Using
594 simplified methods to explore the impact of parameter uncertainty on CO2 storage estimates
595 with application to the Norwegian Continental Shelf. *International Journal of Greenhouse*
596 *Gas Control*, 75:198–213, 8 2018. ISSN 17505836. doi: 10.1016/J.IJGGC.2018.05.017.

597 Mohammad Amin Amooie and Joachim Moortgat. Higher-order black-oil and compositional
598 modeling of multiphase compressible flow in porous media. *International Journal of Multiphase*
599 *Flow*, 105:45–59, 8 2018. ISSN 03019322. doi: 10.1016/J.IJMULTIPHASEFLOW.2018.03.016.

600 O. Andersen, S. E. Gasda, and H. M. Nilsen. Vertically Averaged Equations with Variable
601 Density for CO2 Flow in Porous Media. *Transport in Porous Media*, 107:95–127, 3 2015. ISSN
602 15731634. doi: 10.1007/s11242-014-0427-z.

603 O A Andersen, H M Nilsen, and S E Gasda. Vertical Equilibrium Flow Models with Fully
604 Coupled Geomechanics for CO2 Storage Modeling, Using Precomputed Mechanical Response
605 Functions. *Energy Procedia*, 114:3113–3131, 2017. ISSN 1876-6102. doi: [https://doi.org/](https://doi.org/10.1016/j.egypro.2017.03.1440)
606 [10.1016/j.egypro.2017.03.1440](https://doi.org/10.1016/j.egypro.2017.03.1440). URL [https://www.sciencedirect.com/science/article/](https://www.sciencedirect.com/science/article/pii/S1876610217316259)
607 [pii/S1876610217316259](https://www.sciencedirect.com/science/article/pii/S1876610217316259).

608 Odd Andersen. *Simplified models for numerical simulation of geological CO2 storage*. PhD thesis,
609 2 2017.

610 Susan Anyosa, Jo Eidsvik, and Dario Grana. Evaluating geophysical monitoring strategies for a
611 CO2 storage project. *Computers & Geosciences*, 185:105561, 3 2024. ISSN 0098-3004. doi:
612 [10.1016/J.CAGEO.2024.105561](https://doi.org/10.1016/J.CAGEO.2024.105561). URL [https://www.sciencedirect.com/science/article/](https://www.sciencedirect.com/science/article/pii/S009830042400044X)
613 [pii/S009830042400044X](https://www.sciencedirect.com/science/article/pii/S009830042400044X).

614 Karl W Bandilla, Bo Guo, and Michael A Celia. A guideline for appropriate application of
615 vertically-integrated modeling approaches for geologic carbon storage modeling. *International*
616 *Journal of Greenhouse Gas Control*, 91:102808, 2019. ISSN 1750-5836. doi: [https://doi.org/10.](https://doi.org/10.1016/J.IJGGC.2019.102808)

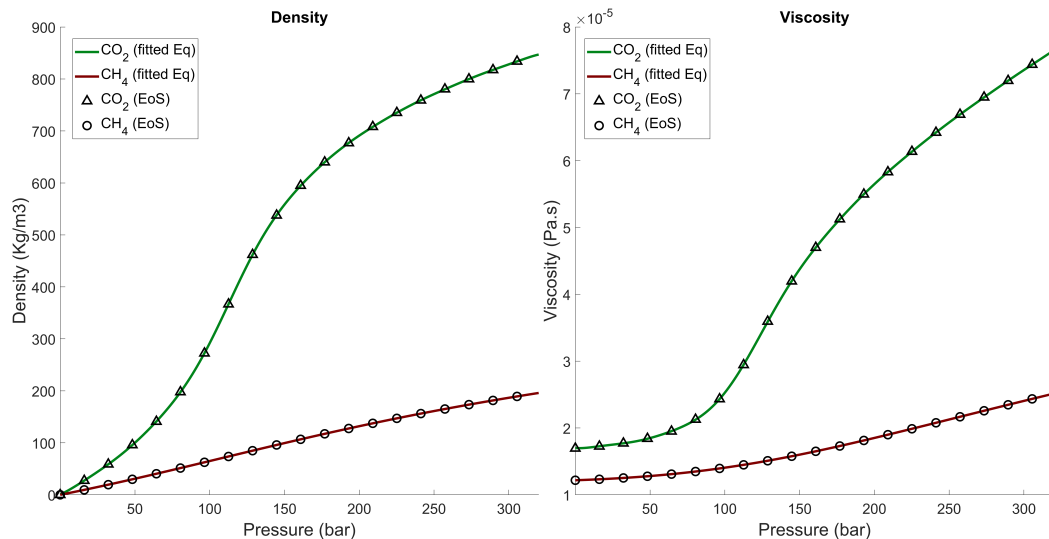


Figure 8: Density and viscosity of CO₂ and methane at T = 60°C, EoS data vs. fitted equation

617 1016/j.ijggc.2019.102808. URL <https://www.sciencedirect.com/science/article/pii/S1750583619300684>.

619 Beatrix Becker, Bo Guo, Karl Bandilla, Michael A. Celia, Bernd Flemisch, and Rainer Helmig.
620 A Pseudo-Vertical Equilibrium Model for Slow Gravity Drainage Dynamics. *Water Resources*
621 *Research*, 53:10491–10507, 12 2017. ISSN 19447973. doi: 10.1002/2017WR021644.

622 Beatrix Becker, Bo Guo, Ivan Buntic, Bernd Flemisch, and Rainer Helmig. An Adaptive Hybrid
623 Vertical Equilibrium/Full-Dimensional Model for Compositional Multiphase Flow. *Water*
624 *Resources Research*, 58(1):e2021WR030990, 2022. ISSN 0043-1397. doi: <https://doi.org/10.1029/2021WR030990>. URL <https://agupubs.onlinelibrary.wiley.com/doi/abs/10.1029/2021WR030990>.

627 Tore I. Bjørnarå, Jan M. Nordbotten, and Joonsang Park. Vertically integrated models for
628 coupled two-phase flow and geomechanics in porous media. *Water Resources Research*, 52:
629 1398–1417, 2 2016. ISSN 19447973. doi: 10.1002/2015WR017290.

630 Andreas Bjørnstad, Eva Halland, and Fridtjof Riis. Evaluation of the CO₂ Storage Potential of
631 the Norwegian Continental Shelf: Online Data Repository. In *Energy Procedia*, volume 114,
632 pages 4394–4399. Elsevier Ltd, 2017. doi: 10.1016/j.egypro.2017.03.1593.

633 Ivan Buntic, Martin Schneider, Bernd Flemisch, and Rainer Helmig. A fully-implicit solving
634 approach to an adaptive multi-scale model - coupling a vertical-equilibrium and full-dimensional
635 model for compressible, multi-phase flow in porous media. *Computational Geosciences*, 29:11,
636 4 2025. ISSN 1420-0597. doi: 10.1007/s10596-025-10351-z.

637 S Y Chen, J F Liu, Q Zhang, F Teng, and B C McLellan. A critical review on deployment
638 planning and risk analysis of carbon capture, utilization, and storage (CCUS) toward carbon
639 neutrality. *Renewable & Sustainable Energy Reviews*, 167, 2022. ISSN 1364-0321. doi:
640 10.1016/j.rser.2022.112537. URL [GotoISI://WOS:000830429400001](https://www.wos.org/doi/abs/10.1016/j.rser.2022.112537).

641 Holger Class, Anozie Ebigbo, Rainer Helmig, Helge K Dahle, Jan M Nordbotten, Michael A
642 Celia, Pascal Audigane, Melanie Darcis, Jonathan Ennis-King, Yaqing Fan, Bernd Flemisch,
643 Sarah E Gasda, Min Jin, Stefanie Krug, Diane Labregere, Ali Naderi Beni, Rajesh J Pawar,
644 Adil Sbai, Sunil G Thomas, Laurent Trenty, and Lingli Wei. A benchmark study on problems

- 645 related to CO₂ storage in geologic formations. *Computational Geosciences*, 13(4):409–434,
646 2009. ISSN 1573-1499. doi: 10.1007/s10596-009-9146-x. URL [https://doi.org/10.1007/
647 s10596-009-9146-x](https://doi.org/10.1007/s10596-009-9146-x).
- 648 B Court, K W Bandilla, M A Celia, A Janzen, M Dobossy, and J M Nordbotten. Applicability
649 of vertical-equilibrium and sharp-interface assumptions in CO₂ sequestration
650 modeling. *International Journal of Greenhouse Gas Control*, 10:134–147, 2012. ISSN 1750-5836.
651 doi: 10.1016/j.ijggc.2012.04.015. URL [GotoISI://WOS:000309790500013](https://www.wos.org/doi/abs/10.1016/j.ijggc.2012.04.015).
- 652 I de Jonge Anderson, H Ramachandran, U Nicholson, S Geiger, A Widyanita, and F Doster.
653 Determining CO₂ storage efficiency within a saline aquifer using reduced complexity mod-
654 els. *Advances in Geo-Energy Research*, 13(1):22–31, 2024. doi: 10.46690/ager.2024.07.
655 04. URL [https://www.scopus.com/inward/record.uri?eid=2-s2.0-85197686714&doi=
656 10.46690%2fager.2024.07.04&partnerID=40&md5=b1a6413ffb543b3b9e168b67dabbacf7](https://www.scopus.com/inward/record.uri?eid=2-s2.0-85197686714&doi=10.46690%2fager.2024.07.04&partnerID=40&md5=b1a6413ffb543b3b9e168b67dabbacf7).
- 657 R Donat, F Guerrero, and P Mulet. Implicit-explicit methods for models for vertical equilibrium
658 multiphase flow. *Computers & Mathematics with Applications*, 68(3):363–383, 2014. ISSN
659 0898-1221. doi: 10.1016/j.camwa.2014.06.006. URL [GotoISI://WOS:000340316100020](https://www.wos.org/doi/abs/10.1016/j.camwa.2014.06.006).
- 660 F. Doster, J. M. Nordbotten, and M. A. Celia. Impact of capillary hysteresis and trapping on
661 vertically integrated models for CO₂ storage. *Advances in Water Resources*, 62:465–474, 12
662 2013. ISSN 03091708. doi: 10.1016/j.advwatres.2013.09.005.
- 663 Florian Doster, Jan M. Nordbotten, and Michael A. Celia. Hysteretic upscaled constitutive
664 relationships for vertically integrated porous media flow. *Computing and Visualization in
665 Science*, 15:147–161, 8 2012. ISSN 14329360. doi: 10.1007/s00791-013-0206-3.
- 666 S E Gasda, J M Nordbotten, and M A Celia. Vertical equilibrium with sub-scale analytical
667 methods for geological CO₂ sequestration. *Computational Geosciences*, 13(4):
668 469–481, 2009. ISSN 1420-0597. doi: 10.1007/s10596-009-9138-x. URL [GotoISI://WOS:
669 000272180000005](https://www.wos.org/doi/abs/10.1007/s10596-009-9138-x).
- 670 S. E. Gasda, J. M. Nordbotten, and M. A. Celia. Vertically averaged approaches for CO₂
671 migration with solubility trapping, 2011. ISSN 00431397.
- 672 Sarah E. Gasda, Halvor M. Nilsen, Helge K. Dahle, and William G. Gray. Effective models for
673 CO₂ migration in geological systems with varying topography. *Water Resources Research*, 48,
674 2012. ISSN 00431397. doi: 10.1029/2012WR012264.
- 675 Sarah E. Gasda, Halvor M. Nilsen, and Helge K. Dahle. Impact of structural heterogeneity on
676 upscaled models for large-scale CO₂ migration and trapping in saline aquifers. *Advances in
677 Water Resources*, 62:520–532, 12 2013a. ISSN 03091708. doi: 10.1016/j.advwatres.2013.05.003.
- 678 Sarah E. Gasda, Elsa du Plessis, and Helge K. Dahle. Upscaled models for CO₂ injection and
679 migration in geological systems. In *Simulation of Flow in Porous Media*, pages 1–38. DE
680 GRUYTER, 10 2013b. doi: 10.1515/9783110282245.1.
- 681 S. Ghanbari, E. J. Mackay, and G. E. Pickup. Measurement of physical dispersion in random
682 correlated permeability fields and its application for upscaling. In *16th European Conference
683 on the Mathematics of Oil Recovery, ECMOR 2018*. European Association of Geoscientists
684 and Engineers, EAGE, 2018. doi: 10.3997/2214-4609.201802200.
- 685 Saeed Ghanbari, Eric J. Mackay, Niklas Heinemann, Juan Alcalde, Alan James, and Michael J.
686 Allen. Impact of CO₂ mixing with trapped hydrocarbons on CO₂ storage capacity and security:
687 A case study from the Captain aquifer (North Sea). *Applied Energy*, 278, 11 2020. ISSN
688 03062619. doi: 10.1016/j.apenergy.2020.115634.

- 689 F. Guerrero, R. Donat, and P. Mulet. Solving a model for 1-D, three-phase flow vertical
690 equilibrium processes in a homogeneous porous medium by means of a Weighted Essentially
691 Non Oscillatory numerical scheme. *Computers and Mathematics with Applications*, 66:1284–
692 1298, 10 2013. ISSN 08981221. doi: 10.1016/j.camwa.2013.07.027.
- 693 B Guo, K W Bandilla, J M Nordbotten, M A Celia, E Keilegavlen, and F Doster. A multiscale
694 multilayer vertically integrated model with vertical dynamics for CO₂ seques-
695 tration in layered geological formations. *Water Resources Research*, 52(8):6490–6505, 2016.
696 ISSN 0043-1397. doi: 10.1002/2016wr018714. URL [GotoISI://WOS:000383684400044](https://doi.org/10.1002/2016wr018714).
- 697 Bo Guo, Karl W. Bandilla, Florian Doster, Eirik Keilegavlen, and Michael A. Celia. A vertically
698 integrated model with vertical dynamics for CO₂ storage. *Water Resources Research*, 50:
699 6269–6284, 8 2014. ISSN 19447973. doi: 10.1002/2013WR015215.
- 700 Bo Guo, Yiheng Tao, Karl Bandilla, and Michael Celia. Vertically Integrated Dual-porosity and
701 Dual-permeability Models for CO₂ Sequestration in Fractured Geological Formation. In *Energy*
702 *Procedia*, volume 114, pages 3343–3352. Elsevier Ltd, 2017. doi: 10.1016/j.egypro.2017.03.1466.
- 703 M. Haajizadeh, F. J. Fayers, A. P. Cockin, M. Roffey, and D. J. Bond. On the Importance
704 of Dispersion and Heterogeneity in the Compositional Simulation of Miscible Gas Processes.
705 Society of Petroleum Engineers (SPE), 10 1999. doi: 10.2118/57264-ms.
- 706 A Hamza, I A Hussein, M J Al-Marri, M Mahmoud, R Shawabkeh, and S Aparicio.
707 CO₂ enhanced gas recovery and sequestration in depleted gas reservoirs:
708 A review. *Journal of Petroleum Science and Engineering*, 196, 2021. ISSN 0920-4105. doi:
709 10.1016/j.petrol.2020.107685. URL [GotoISI://WOS:000600808100054](https://doi.org/10.1016/j.petrol.2020.107685).
- 710 Hassan Hassanzadeh, Mehran Pooladi-Darvish, Adel M. Elsharkawy, David W. Keith, and Yuri
711 Leonenko. Predicting PVT data for CO₂-brine mixtures for black-oil simulation of CO₂
712 geological storage. *International Journal of Greenhouse Gas Control*, 2(1):65–77, 2008. ISSN
713 17505836. doi: 10.1016/S1750-5836(07)00010-2.
- 714 R. P. Hepple and S. M. Benson. Geologic storage of carbon dioxide as a climate change mitigation
715 strategy: performance requirements and the implications of surface seepage. *Environmental*
716 *Geology 2004 47:4*, 47(4):576–585, 11 2004. ISSN 1432-0495. doi: 10.1007/S00254-004-1181-2.
717 URL <https://link.springer.com/article/10.1007/s00254-004-1181-2>.
- 718 Charles R Jenkins, Peter J Cook, Jonathan Ennis-King, James Undershultz, Chris Boreham,
719 Tess Dance, Patrice de Caritat, David M Etheridge, Barry M Freifeld, Allison Hortle, Dirk
720 Kirste, Lincoln Paterson, Roman Pevzner, Ulrike Schacht, Sandeep Sharma, Linda Stalker,
721 and Milovan Urosevic. Safe storage and effective monitoring of CO₂ in depleted
722 gas fields. *Proceedings of the National Academy of Sciences*, 109(2):E35–E41, 2012. doi:
723 1073/pnas.1107255108. URL <https://www.pnas.org/doi/abs/10.1073/pnas.1107255108>.
- 724 Samuel Krevor, Heleen de Coninck, Sarah E Gasda, Navraj Singh Ghaleigh, Vincent de Gooyert,
725 Hadi Hajibeygi, Ruben Juanes, Jerome Neufeld, Jennifer J Roberts, and Floris Swennenhuis.
726 Subsurface carbon dioxide and hydrogen storage for a sustainable energy future. *Nature Reviews*
727 *Earth & Environment*, 4(2):102–118, 2023. ISSN 2662-138X. doi: 10.1038/s43017-022-00376-8.
728 URL <https://doi.org/10.1038/s43017-022-00376-8>.
- 729 Ajitabh Kumar, Robin Ozah, Myeong Noh, Gary A. Pope, Steven Bryant, Kamy Sepahmoori,
730 and Larry W. Lake. Reservoir Simulation of CO₂ Storage in Deep Saline Aquifers. *SPE*
731 *Journal*, 10(03):336–348, 9 2005. ISSN 1086-055X. doi: 10.2118/89343-PA. URL <https://dx.doi.org/10.2118/89343-PA>.

- 733 H C Lau, S Ramakrishna, K Zhang, and A V Radhamani. The Role of Carbon Capture and
734 Storage in the Energy Transition. *Energy & Fuels*, 35(9):7364–7386, 2021. ISSN 0887-0624.
735 doi: 10.1021/acs.energyfuels.1c00032. URL [GotoISI://WOS:000648878900028](https://doi.org/10.1021/acs.energyfuels.1c00032).
- 736 Knut-Andreas Lie. *An Introduction to Reservoir Simulation Using MATLAB/GNU Octave:
737 User Guide for the MATLAB Reservoir Simulation Toolbox (MRST)*. Cambridge University
738 Press, Cambridge, 2019. ISBN 9781108492430. doi: DOI:10.1017/9781108591416. URL
739 <https://www.cambridge.org/core/product/F48C3D8C88A3F67E4D97D4E16970F894>.
- 740 Knut-Andreas Lie and Olav Møyner. *Advanced Modeling with the MATLAB Reservoir Sim-
741 ulation Toolbox*. Cambridge University Press, Cambridge, 2021. ISBN 9781316519967.
742 doi: DOI:10.1017/9781009019781. URL [https://www.cambridge.org/core/product/
743 7AC2425C73F6F729DB88DB1A504FA1E7](https://www.cambridge.org/core/product/7AC2425C73F6F729DB88DB1A504FA1E7).
- 744 Shezhan Liu, Lei Yuan, Changzhong Zhao, Yi Zhang, and Yongchen Song. A review of research
745 on the dispersion process and CO₂ enhanced natural gas recovery in depleted gas reservoir, 1
746 2022. ISSN 09204105.
- 747 Jianli Ma, Qi Li, Thomas Kempka, and Michael Kühn. Hydromechanical Response and Impact
748 of Gas Mixing Behavior in Subsurface CH₄ Storage with CO₂-Based Cushion Gas. *Energy &
749 Fuels*, 33(7):6527–6541, 7 2019. ISSN 0887-0624. doi: 10.1021/acs.energyfuels.9b00518. URL
750 <https://doi.org/10.1021/acs.energyfuels.9b00518>.
- 751 Rafael March Castaneda Neto. Modelling of CO₂ storage in naturally fractured reservoirs, 2018.
752 URL <http://hdl.handle.net/10399/3516>.
- 753 Carlos Méndez, Nicholas Simpson, Francis Johnson, and Arlene Birt. *Climate Change 2023:
754 Synthesis Report (Full Volume) Contribution of Working Groups I, II and III to the Sixth
755 Assessment Report of the Intergovernmental Panel on Climate Change*. 7 2023. doi: 10.59327/
756 IPCC/AR6-9789291691647.
- 757 O. Moyner. JutulDarcy.jl - a Fully Differentiable High-Performance Reservoir Simulator based on
758 Automatic Differentiation. In *ECMOR 2024*, volume 2024, pages 1–37. European Association
759 of Geoscientists & Engineers, 9 2024. doi: 10.3997/2214-4609.202437111. URL [https:
760 //www.earthdoc.org/content/papers/10.3997/2214-4609.202437111](https://www.earthdoc.org/content/papers/10.3997/2214-4609.202437111).
- 761 O Moyner and H M Nilsen. Multiresolution coupled vertical equilibrium model for fast flexible
762 simulation of CO₂ storage. *Computational Geosciences*, 23(1):1–20, 2019. ISSN
763 1420-0597. doi: 10.1007/s10596-018-9775-z. URL [GotoISI://WOS:000459423400001](https://doi.org/10.1007/s10596-018-9775-z).
- 764 N S Muhammed, M B Haq, D A Al Shehri, A Al-Ahmed, M M Rahman, E Zaman, and S Iglauer.
765 Hydrogen storage in depleted gas reservoirs: A comprehensive review. *FUEL*, 337, 2023. ISSN
766 0016-2361. doi: 10.1016/j.fuel.2022.127032.
- 767 Trine S. Mykkeltvedt and Jan M. Nordbotten. Estimating effective rates of convective mixing
768 from commercial-scale injection. *Environmental Earth Sciences*, 67:527–535, 9 2012. ISSN
769 18666280. doi: 10.1007/s12665-012-1674-3.
- 770 H M Nilsen, K A Lie, and O Andersen. Fully-implicit simulation of vertical-equilibrium models
771 with hysteresis and capillary fringe. *Computational Geosciences*, 20(1):49–67, 2016a. ISSN
772 1420-0597. doi: 10.1007/s10596-015-9547-y. URL [GotoISI://WOS:000373347600004](https://doi.org/10.1007/s10596-015-9547-y).
- 773 H M Nilsen, K A Lie, and O Andersen. Robust simulation of sharp-interface models for fast
774 estimation of CO₂ trapping capacity in large-scale aquifer systems. *Computa-
775 tional Geosciences*, 20(1):93–113, 2016b. ISSN 1420-0597. doi: 10.1007/s10596-015-9549-9.
776 URL [GotoISI://WOS:000373347600006](https://doi.org/10.1007/s10596-015-9549-9).

- 777 J. M. Nordbotten and H. K. Dahle. Impact of the capillary fringe in vertically integrated
778 models for CO₂ storage. *Water Resources Research*, 47, 2011. ISSN 00431397. doi: 10.1029/
779 2009WR008958.
- 780 Jan Nordbotten and Michael Celia. Geological Storage of CO₂: Modeling Approaches for Large-
781 Scale Simulation. *Geological Storage of CO₂: Modeling Approaches for Large-Scale Simulation*,
782 pages i–ix, 11 2011. ISSN 9780470889466. doi: 10.1002/9781118137086.fmatter.
- 783 C M Oldenburg, K Pruess, and S M Benson. Process Modeling of CO₂ Injection into Natural
784 Gas Reservoirs for Carbon Sequestration and Enhanced Gas Recovery. *Energy & Fuels*, 15(2):
785 293–298, 3 2001. ISSN 0887-0624. doi: 10.1021/ef000247h. URL [https://doi.org/10.1021/
786 ef000247h](https://doi.org/10.1021/ef000247h).
- 787 Curtis M Oldenburg and Escholarship Org. Carbon sequestration in natural gas reservoirs:
788 enhanced gas recovery and natural gas storage. 2003. URL [https://escholarship.org/
789 content/qt61b1p0gk/qt61b1p0gk.pdf](https://escholarship.org/content/qt61b1p0gk/qt61b1p0gk.pdf).
- 790 Milan J Patel, Eric F May, and Michael L Johns. High-fidelity reservoir simulations of enhanced
791 gas recovery with supercritical CO₂. *Energy*, 111:548–559, 2016. ISSN 0360-5442. doi: <https://doi.org/10.1016/j.energy.2016.04.120>. URL [https://www.sciencedirect.com/science/
792 //doi.org/10.1016/j.energy.2016.04.120](https://www.sciencedirect.com/science/article/pii/S0360544216305400). URL [https://www.sciencedirect.com/science/
793 article/pii/S0360544216305400](https://www.sciencedirect.com/science/article/pii/S0360544216305400).
- 794 Per Pettersson, Svenn Tveit, and Sarah E. Gasda. Dynamic estimates of extreme-case CO₂
795 storage capacity for basin-scale heterogeneous systems under geological uncertainty. *Inter-
796 national Journal of Greenhouse Gas Control*, 116:103613, 5 2022. ISSN 1750-5836. doi:
797 10.1016/J.IJGGC.2022.103613. URL [https://www.sciencedirect.com/science/article/
798 pii/S1750583622000329](https://www.sciencedirect.com/science/article/pii/S1750583622000329).
- 799 Hariharan Ramachandran, Iain de Jonge-Anderson, Ikhwanul Hafizi Musa, Uisdean Nicholson,
800 Chee Phuat Tan, Sebastian Geiger, and Florian Doster. Rapid Fault Leakage Modeling for
801 CO₂ Storage in Saline Aquifers. 8 2024. doi: 10.31223/X5S12N. URL [https://eartharxiv.
802 org/repository/view/7535/](https://eartharxiv.org/repository/view/7535/).
- 803 Philip S. Ringrose, Anne Kari Furre, Stuart M.V. Gilfillan, Samuel Krevor, Martin Landroslash,
804 Rory Leslie, Tip Meckel, Bamshad Nazarian, and Adeel Zahid. Storage of Carbon Dioxide in
805 Saline Aquifers: Physicochemical Processes, Key Constraints, and Scale-Up Potential. *Annual
806 Review of Chemical and Biomolecular Engineering*, 12:471–494, 6 2021. ISSN 19475446. doi:
807 10.1146/ANNUREV-CHEMBIOENG-093020-091447,. URL [https://pubmed.ncbi.nlm.nih.
808 gov/33872518/](https://pubmed.ncbi.nlm.nih.gov/33872518/).
- 809 Lorenzo Rosa and Marco Mazzotti. Potential for hydrogen production from sustainable biomass
810 with carbon capture and storage. *Renewable and Sustainable Energy Reviews*, 157:112123,
811 2022. ISSN 1364-0321. doi: <https://doi.org/10.1016/j.rser.2022.112123>. URL [https://www.
812 sciencedirect.com/science/article/pii/S136403212200051X](https://www.sciencedirect.com/science/article/pii/S136403212200051X).
- 813 Vijay Kumar Shrivastava. Physical Dispersion in Compositional Reservoir Simulation. Technical
814 report, 2003. URL <http://hdl.handle.net/1880/39841>.
- 815 Amine Tadjer, Aojie Hong, and Reidar B. Bratvold. A sequential decision and data ana-
816 lytics framework for maximizing value and reliability of CO₂ storage monitoring. *Jour-
817 nal of Natural Gas Science and Engineering*, 96:104298, 12 2021. ISSN 1875-5100. doi:
818 10.1016/J.JNGSE.2021.104298. URL [https://www.sciencedirect.com/science/article/
819 pii/S1875510021004959](https://www.sciencedirect.com/science/article/pii/S1875510021004959).

- 820 Yiheng Tao, Bo Guo, Karl W. Bandilla, and Michael A. Celia. Vertically integrated dual-
821 continuum models for CO₂ injection in fractured geological formations. *Computational*
822 *Geosciences*, 23:273–284, 4 2019. ISSN 15731499. doi: 10.1007/s10596-018-9805-x.
- 823 George A. Virnovsky, Hans Martin Helset, and Svein M. Skjæveland. Stability of displacement
824 fronts in WAG operations. *SPE Journal*, 1:383–393, 1996. ISSN 1086055X. doi: 10.2118/
825 28622-pa.
- 826 Christopher J. Wareing, Michael Fairweather, Samuel A.E.G. Falle, and Robert M. Woolley.
827 Validation of a model of gas and dense phase CO₂ jet releases for carbon capture and storage
828 application. *International Journal of Greenhouse Gas Control*, 20:254–271, 2014. ISSN
829 17505836. doi: 10.1016/j.ijggc.2013.11.012.
- 830 B Wei, B W Wang, X Li, M Aishan, and Y Ju. CO₂ storage in depleted oil and
831 gas reservoirs: A review. *Advances in Geo-Energy Research*, 9(2):76–93, 2023. ISSN 2207-9963.
832 doi: 10.46690/ager.2023.08.02. URL [GotoISI://WOS:001054316800002](https://www.wos.org/doi/10.46690/ager.2023.08.02).
- 833 Tianyuan Zheng, Bo Guo, and Haibing Shao. A hybrid multiscale framework coupling multilayer
834 dynamic reconstruction and full-dimensional models for CO₂ storage in deep saline aquifers.
835 *Journal of Hydrology*, 600, 9 2021. ISSN 00221694. doi: 10.1016/j.jhydrol.2021.126649.